

# Bound-Constrained Sparse Representation for Electrical Impedance Tomography

Chun Zhang and Dong Liu, *Senior Member, IEEE*

**Abstract**—This study proposes a bound-constrained sparse representation (BC-SR) framework for electrical impedance tomography (EIT), aimed at improving conductivity estimation without explicit regularization. BC-SR adopts a representation-driven strategy, generating conductivity from low-dimensional latent variables via an implicit composite parameterization. Structural priors are embedded using a truncated graph-Laplacian basis, while a bound-preserving nonlinear mapping enforces admissible conductivity ranges and improves conditioning through implicit gradient modulation. The approach ensures robust convergence, even under noisy or incomplete data. Extensive validation on 2D/3D simulations, tank experiments, and in-vivo lung data shows that BC-SR improves physical consistency and structural fidelity, offering enhanced robustness compared to traditional methods. Additionally, BC-SR enables 3D time-difference EIT reconstruction, offering improved spatial resolution and a more coherent representation of 3D conductivity distributions, particularly for in-vivo lung data. This suggests potential for improved performance in EIT, particularly in clinical applications for respiratory monitoring.

**Index Terms**—Implicit Parameterization, Sparse Representation, Three-Dimensional Imaging, Lung Ventilation, Electrical Impedance Tomography

## I. INTRODUCTION

**E**LECTRICAL impedance tomography (EIT) is a non-invasive imaging modality with advantages including the absence of ionizing radiation, low cost, and high temporal resolution, making it suitable for real-time bedside monitoring in applications such as lung and cardiac function assessment [1]–[4]. Despite these advantages, obtaining accurate and reliable reconstructions in practical settings remains challenging.

This challenge arises from two fundamental aspects: the highly nonlinear relationship between boundary measurements and internal conductivity, and the severe ill-posedness of the inverse problem [5]. As a result, the reconstruction is highly sensitive to measurement noise and modeling errors [6].

To alleviate this difficulty, linearized approaches are commonly adopted, where measurements are interpreted relative to a reference state and the forward model is expanded around

a baseline conductivity, yielding a stabilized linear inverse problem. This formulation underlies classical methods such as NOSER [7] and GREIT [8], [9]. Owing to their robustness to modeling uncertainties, such methods are widely used in differential imaging formulations.

In contrast, when no reference state is available, absolute EIT aims to reconstruct conductivity directly from a single set of measurements by solving a nonlinear data-misfit minimization problem. The resulting ill-posedness is commonly addressed through explicit regularization, including total variation, Laplacian smoothing, and Bayesian priors [10]–[12], with further improvements achieved via structured sparsity and hierarchical Bayesian modeling [13], [14]. While effective, these formulations rely on externally imposed priors, leading to a trade-off between data fidelity and prior assumptions and requiring careful tuning of regularization parameters.

These limitations motivate alternative formulations in which prior knowledge is incorporated directly into the conductivity representation, rather than enforced through explicit regularization. From this perspective, representation-driven methods constrain the solution space to a structured low-dimensional manifold. Early approaches include analytic transforms such as DCT/DWT and orthogonal polynomial bases, as well as learned dictionaries (e.g., K-SVD) [15]–[18], which provide compact representations but remain fundamentally linear and thus limited in capturing complex conductivity variations.

To improve expressiveness, explicit or implicit representation strategies have been well explored, extending classical simple parameterizations to more flexible and structure-aware representations. A representative class includes shape-based methods [19]–[21], which describe conductivity through implicit geometric evolution and are particularly suited for piecewise-constant or boundary-dominated structures. Another line of work employs localized basis expansions, such as Gaussian-type kernels [22], which provide spatial adaptivity while enforcing smoothness and locality via explicit basis construction.

Moving beyond explicitly constructed representations, more general parameterizations have been developed based on learning-based models. A representative class includes variational autoencoders (VAEs) [23], [24], which learn low-dimensional latent representations that capture high-level features of EIT images, enabling compact and data-driven parameterizations of conductivity. More broadly, conductivity can be modeled through implicit neural representations, where Deep image prior (DIP)-style frameworks and coordinate-based networks with positional encoding [25]–[27] parameterize conductivity via network weights and architectural bias,

This work was supported by the National Natural Science Foundation of China under Grant 62371433.

C. Zhang and D. Liu are with the School of Biomedical Engineering and Suzhou Institute for Advanced Research, University of Science and Technology of China, Suzhou 215123, China. Corresponding author: Dong Liu (e-mail: dong.liu@outlook.com).

D. Liu is also with the Laboratory of Spin Magnetic Resonance and Anhui Province Key Laboratory of Scientific Instrument Development and Application, University of Science and Technology of China, Hefei 230026, China, and with the Jiangsu Provincial Key Laboratory of Multimodal Digital Twin Technology, Suzhou 215123, China.

D. Liu is also with the Institute of Quantum Sensing of WuXi, Wuxi 214100, China.

allowing regularization of the inverse problem without explicit training data. Physics-informed neural networks (PINNs) [28]–[30] further incorporate governing equations through PDE residual minimization to enforce physical consistency with the forward model. Despite their enhanced representational capacity, these approaches often rely on complex network architectures, resulting in high computational cost and sensitivity to initialization. In addition, when strong data-driven priors are imposed, the reconstruction may be dominated by the learned representation, effectively reducing the influence of the data fidelity term and limiting robustness under modeling uncertainties.

To address these limitations, we propose a bound-constrained sparse representation (BC-SR) framework for EIT, which introduces a composite nonlinear parameterization that generates conductivity from low-dimensional latent variables. Structural priors are incorporated via a truncated graph-Laplacian basis, while admissible conductivity ranges are enforced through an implicit nonlinear mapping. This formulation restricts the solution space to physically plausible configurations and enables efficient latent-space optimization using a damped Gauss–Newton scheme, providing a unified framework for both absolute and time-difference imaging.

The main contributions of this work are summarized as follows:

- **BC-SR Framework:** We propose a bound-constrained sparse representation framework that integrates structural priors and physical feasibility into a unified nonlinear parameterization of conductivity.
- **Unified Representation across Imaging Regimes:** We develop a single conductivity representation that is applicable to both absolute and time-difference EIT, enabling consistent reconstruction under modeling uncertainties within a unified optimization framework.
- **Comprehensive Validation:** The proposed method is validated on 2D/3D simulations, tank experiments, and in-vivo data, demonstrating improved structural fidelity, physical consistency, and robustness compared with conventional approaches.

The remainder of this paper is organized as follows. Section II reviews the forward model; Section III presents the proposed method; Section IV describes the experimental setup; Sections V and VI report numerical and experimental results; Sections VII and VIII conclude the paper, with the former focusing on analysis and limitations, and the latter summarizing the work and outlining potential extensions.

## II. FORWARD MODEL OF ELECTRICAL IMPEDANCE TOMOGRAPHY

EIT aims to recover the internal conductivity distribution  $\kappa(\mathbf{x})$  inside a domain  $\Omega$  from boundary voltage measurements induced by applied currents. Let  $L$  electrodes be attached to  $\partial\Omega$ , and the governing equations are described by the complete electrode model (CEM) [31]:

$$\begin{aligned} \nabla \cdot (\kappa(\mathbf{x}) \nabla \phi(\mathbf{x})) &= 0, & \mathbf{x} \in \Omega, \\ \phi + z_q \kappa \frac{\partial \phi}{\partial \boldsymbol{\nu}} &= U_q, & \mathbf{x} \in e_q, \quad q = 1, \dots, L, \\ \int_{e_q} \kappa \frac{\partial \phi}{\partial \boldsymbol{\nu}} dS &= I_q, & q = 1, \dots, L, \\ \kappa \frac{\partial \phi}{\partial \boldsymbol{\nu}} &= 0, & \mathbf{x} \in \partial\Omega \setminus \bigcup_{q=1}^L e_q. \end{aligned} \quad (1)$$

where  $\phi$  denotes the electric potential,  $U_q$  and  $I_q$  are electrode voltages and currents, and  $z_q$  is the contact impedance. The standard charge conservation and reference potential constraints are imposed:

$$\sum_{q=1}^L I_q = 0, \quad \sum_{q=1}^L U_q = 0.$$

In the finite element discretization [32], the conductivity field is represented by a nodal vector  $\boldsymbol{\sigma} \in \mathbb{R}^N$ , where  $N$  is the number of nodes in the FEM mesh.

The discrete forward model is given by

$$\mathbf{V} = \mathcal{U}(\boldsymbol{\sigma}) + \mathbf{e}, \quad (2)$$

where  $\mathbf{V}$  denotes the measured electrode voltages and  $\mathbf{e}$  is measurement noise.

## III. THE PROPOSED BC-SR FRAMEWORK

### A. Inverse Problem Formulation

Given boundary measurements  $\mathbf{V}$  and the discrete forward mapping  $\mathcal{U}(\cdot)$ , EIT reconstruction aims to estimate the conductivity field  $\boldsymbol{\sigma}$  by solving a bound-constrained nonlinear least-squares problem

$$\hat{\boldsymbol{\sigma}} = \arg \min_{\boldsymbol{\sigma}} \frac{1}{2} \|\mathcal{U}(\boldsymbol{\sigma}) - \mathbf{V}\|_2^2 \quad \text{s.t.} \quad \boldsymbol{\ell} \leq \boldsymbol{\sigma} \leq \mathbf{u}. \quad (3)$$

Here,  $\boldsymbol{\ell}$  and  $\mathbf{u}$  denote element-wise lower and upper bound vectors, respectively. In this work, we assume a spatially uniform admissible conductivity range  $[\boldsymbol{\ell}, \mathbf{u}]$  over the entire domain, such that  $\boldsymbol{\ell} = (\ell, \dots, \ell)^\top$  and  $\mathbf{u} = (u, \dots, u)^\top$ .

Directly solving (3) requires handling bound constraints explicitly during optimization, which can complicate the solution process. To address this, we adopt an implicit nonlinear parameterization that encodes the admissible conductivity range directly into the model. Specifically, the conductivity is represented as

$$\boldsymbol{\sigma} = \mathcal{H}(\mathbf{c}), \quad \mathbf{c} = \mathbf{B}\boldsymbol{\alpha}, \quad (4)$$

where  $\mathcal{H}(\cdot)$  is a nonlinear mapping that enforces the prescribed bounds,  $\mathbf{B}$  is a fixed structural basis, and  $\boldsymbol{\alpha}$  is a reduced coefficient vector.

With this parameterization, the bound constraints are satisfied by construction, and the original constrained problem is transformed into an unconstrained optimization problem in the reduced latent space:

$$\hat{\boldsymbol{\alpha}} = \arg \min_{\boldsymbol{\alpha}} \frac{1}{2} \|\mathcal{U}(\mathcal{H}(\mathbf{B}\boldsymbol{\alpha})) - \mathbf{V}\|_2^2. \quad (5)$$

The conductivity field is then recovered as  $\hat{\sigma} = \mathcal{H}(\mathbf{B}\hat{\alpha})$ . This formulation embeds physical feasibility directly into the parameterization while reducing the dimensionality of the optimization problem. In the following, we introduce the nonlinear mapping  $\mathcal{H}(\cdot)$  that enforces the admissible range, followed by the construction of the structural basis  $\mathbf{B}$  for low-dimensional representation.

### B. Nonlinear Bound Mapping

The nonlinear mapping  $\mathcal{H}(\cdot)$  enforces the admissible conductivity range in a physically consistent manner. Specifically,

$$\mathcal{H}(\mathbf{c}) = \boldsymbol{\ell} + (\mathbf{u} - \boldsymbol{\ell}) \odot f(\mathbf{c} + \Delta\mathbf{c}), \quad (6a)$$

$$f(z) = \frac{1}{1 + e^{-z}}, \quad (6b)$$

where  $\odot$  denotes element-wise multiplication. By construction,  $\mathcal{H}(\mathbf{c}) \in [\boldsymbol{\ell}, \mathbf{u}]$ .

To ensure consistency with a prescribed initial conductivity  $\boldsymbol{\sigma}^0 \in [\boldsymbol{\ell}, \mathbf{u}]$ , the shift  $\Delta\mathbf{c}$  is chosen such that

$$\mathcal{H}(\mathbf{0}) = \boldsymbol{\sigma}^0, \quad (7)$$

which yields

$$\Delta\mathbf{c} = \log\left(\frac{\boldsymbol{\sigma}^0 - \boldsymbol{\ell}}{\mathbf{u} - \boldsymbol{\sigma}^0}\right), \quad (8)$$

with all operations applied componentwise.

In the absence of prior information, we adopt a homogeneous initialization  $\boldsymbol{\sigma}_{\text{homo}}$  and estimate a global scaling factor

$$s = \frac{\sum_i V_i^2}{\sum_i [\mathcal{U}(\boldsymbol{\sigma}_{\text{homo}})]_i V_i}, \quad (9)$$

so that  $\boldsymbol{\sigma}^0 = s \boldsymbol{\sigma}_{\text{homo}}$ .

The mapping  $\mathcal{H}$  also modulates the update sensitivity. Its derivative is given by

$$\mathcal{H}'(\mathbf{c}) = \text{diag}\left(\frac{(\boldsymbol{\sigma} - \boldsymbol{\ell}) \odot (\mathbf{u} - \boldsymbol{\sigma})}{\mathbf{u} - \boldsymbol{\ell}}\right), \quad (10)$$

which naturally damps updates near the bounds and improves numerical stability.

Importantly, this formulation provides a unified framework for both absolute and time-difference imaging. In the difference imaging setting, let  $\boldsymbol{\sigma}_0$  and  $\boldsymbol{\sigma}_1$  denote the baseline and target states. By selecting  $\Delta\mathbf{c}$  such that  $\mathcal{H}(\mathbf{0}) = \boldsymbol{\sigma}_0$ , the reconstruction is naturally warm-started as

$$\boldsymbol{\sigma}_1^{(0)} = \boldsymbol{\sigma}_0. \quad (11)$$

Under this formulation, the reconstruction updates deviations from a physically consistent baseline, thereby reducing the impact of modeling errors and enabling robust time-difference imaging within the same optimization framework.

### C. Graph Laplacian-based Sparse Representation

Within the BC-SR framework, the linear basis  $\mathbf{B}$  encodes the structural prior of the conductivity field. On an FEM mesh, a natural choice is to exploit node connectivity. We construct an undirected graph from the mesh nodes, with adjacency matrix  $\mathbf{W}$  defined by

$$w_{ij} = \begin{cases} 1, & \text{if nodes } i \text{ and } j \text{ are connected,} \\ 0, & \text{otherwise.} \end{cases} \quad (12)$$

This unweighted connectivity-based construction avoids introducing additional tuning parameters while preserving the mesh topology. The corresponding graph Laplacian is

$$\mathbf{L} = \mathbf{D} - \mathbf{W}, \quad \mathbf{D} = \text{diag}\left(\sum_j w_{ij}\right), \quad (13)$$

where the sum is taken over all nodes connected to node  $i$ .

The Laplacian matrix  $\mathbf{L}$  is symmetric positive semidefinite and admits the eigen-decomposition

$$\mathbf{L} = \mathbf{G}\mathbf{\Lambda}\mathbf{G}^\top, \quad (14)$$

where the columns of  $\mathbf{G}$  are orthonormal eigenvectors, ordered according to increasing eigenvalues in  $\mathbf{\Lambda}$ . In practice, these eigenvectors are obtained by solving the standard symmetric eigenvalue problem associated with  $\mathbf{L}$ . Since  $\mathbf{L}$  is sparse and constructed purely from mesh connectivity, efficient numerical solvers can be directly applied. Eigenvectors corresponding to the smallest eigenvalues capture smooth, low-frequency modes on the mesh. We therefore define

$$\mathbf{B} := \mathbf{G}_{N_b}, \quad (15)$$

where  $\mathbf{G}_{N_b} \in \mathbb{R}^{N \times N_b}$  contains the first  $N_b$  eigenvectors ( $N_b \ll N$ ). This effectively performs a low-frequency dimensionality reduction on the mesh, analogous to DCT or other standard transforms for regular grids.

Importantly, this construction is dimension-independent. For both 2D and 3D meshes, the graph Laplacian is assembled in the same manner from node connectivity, and the corresponding eigenvectors are computed using the same procedure. The only difference lies in the mesh structure itself, not in the formulation. Therefore, the proposed basis construction generalizes naturally to arbitrary geometries and unstructured meshes (see Fig. 1).

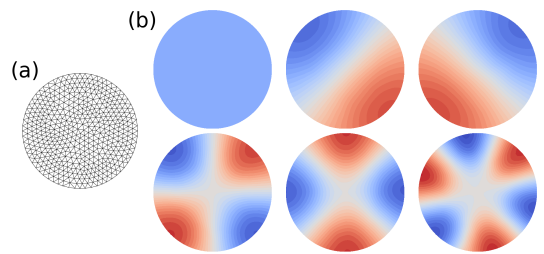


Fig. 1. (a) Finite element mesh. (b) The first six Laplacian eigenvectors illustrating smooth, low-frequency graph modes.

### D. Optimization Algorithm

The BC-SR objective function defined in (5) is solved using the Levenberg–Marquardt–Fletcher (LMF) algorithm [33], a standard method for nonlinear least-squares optimization.

We define the residual as

$$\mathbf{r} = \mathcal{U}(\boldsymbol{\sigma}) - \mathbf{V},$$

where  $\mathbf{r} \in \mathbb{R}^M$ ,  $\boldsymbol{\sigma} \in \mathbb{R}^N$ , and  $\mathbf{V} \in \mathbb{R}^M$ . By the chain rule, the Jacobian with respect to  $\boldsymbol{\alpha}$  is given by

$$\mathcal{J}_\alpha = \mathcal{J}_\sigma \mathcal{H}'(\mathbf{c}) \mathbf{B}, \quad (16)$$

where  $\mathcal{J}_\sigma = \frac{\partial \mathbf{r}}{\partial \boldsymbol{\sigma}} \in \mathbb{R}^{M \times N}$ ,  $\mathcal{H}'(\mathbf{c}) \in \mathbb{R}^{N \times N}$  is diagonal, and  $\mathbf{B} \in \mathbb{R}^{N \times N_b}$ . Accordingly,  $\mathcal{J}_\alpha \in \mathbb{R}^{M \times N_b}$ .

The gradient and Gauss–Newton approximation of the Hessian are

$$\nabla \mathcal{L}(\boldsymbol{\alpha}) = \mathcal{J}_\alpha^\top \mathbf{r}, \quad (17a)$$

$$\mathbf{H}(\boldsymbol{\alpha}) = \mathcal{J}_\alpha^\top \mathcal{J}_\alpha + \mu \mathbf{I}, \quad (17b)$$

where  $\mu > 0$  is a damping parameter,  $\mathbf{I} \in \mathbb{R}^{N_b \times N_b}$  is the identity matrix.

At iteration  $k$ , the update direction  $\mathbf{d}$  is obtained from

$$(\mathcal{J}_\alpha^\top \mathcal{J}_\alpha + \mu_k \mathbf{I}) \mathbf{d} = -\mathcal{J}_\alpha^\top \mathbf{r}. \quad (18)$$

The step is accepted based on the ratio of actual to predicted reduction,

$$\rho_k = \frac{\mathcal{L}(\boldsymbol{\alpha}^k) - \mathcal{L}(\boldsymbol{\alpha}^k + \mathbf{d})}{m_k(\mathbf{0}) - m_k(\mathbf{d})}, \quad (19)$$

and the damping parameter is updated following Fletcher’s rule

$$\mu_{k+1} = \begin{cases} \gamma_2 \mu_k, & \rho_k < \rho_1, \\ \gamma_1 \mu_k, & \rho_k > \rho_2, \\ \mu_k, & \text{otherwise.} \end{cases} \quad (20)$$

### E. Implementation Details

For clarity, we distinguish between the LMF-related hyperparameters  $\{\mu_0, \gamma_1, \gamma_2, \rho_1, \rho_2\}$ , which govern the damping and trust-region updates, and the stopping parameters, namely  $T_{\max}$  and  $\varepsilon$ , which control the maximum number of iterations and the minimum step size, respectively. Unless otherwise stated, we adopt standard textbook values for the LMF algorithm,

$$\rho_1 = 0.25, \quad \rho_2 = 0.75, \quad \gamma_1 = 0.25, \quad \gamma_2 = 4,$$

and initialize the damping parameter with a small value  $\mu_0$  (e.g.,  $\mu_0 = 10^{-4}$ ), which effectively starts the iterations in the Gauss–Newton regime. These values are not tuned in our experiments and are kept identical across all 2D and 3D settings (Sections IV-C and IV-D), consistent with standard practice and the well-known robustness of the LMF algorithm.

The latent variables are initialized as  $\boldsymbol{\alpha}^0 = \mathbf{0}$ , which yields a homogeneous latent field  $\mathbf{c}^0 = \mathbf{0}$  and a physically admissible background conductivity  $\boldsymbol{\sigma}^0$  defined in (9). The outer iterations are terminated when either the maximum iteration count  $T_{\max}$  is reached or the step norm  $\|\mathbf{d}^k\|$  falls below a prescribed tolerance  $\varepsilon$ . The complete BC-SR reconstruction procedure is summarized in Algorithm 1.

---

### Algorithm 1: BC-SR Reconstruction Algorithm

---

**Input:** Measurements  $\mathbf{V}$ , forward operator  $\mathcal{U}$

**Input:** Graph basis  $\mathbf{B}$ , physical bounds  $(\ell, u)$

**Input:** Hyperparameters

$$\Theta = \{T_{\max}, \varepsilon, \mu_0, \gamma_1, \gamma_2, \rho_1, \rho_2\}$$

**Output:** Reconstructed conductivity  $\hat{\boldsymbol{\sigma}}$

1 **Initialization:**  $\boldsymbol{\alpha}^0 = \mathbf{0}$ ;  $\mathbf{c}^0 = \mathbf{0}$ ;  $\boldsymbol{\sigma}^0$  given by (9);

$\mu_k \leftarrow \mu_0$ ;  $k \leftarrow 0$ ;

2 **while**  $k < T_{\max}$  **and**  $\|\mathbf{d}^k\| > \varepsilon$  **do**

3   Compute residual  $\mathbf{r}^k = \mathcal{U}(\boldsymbol{\sigma}^k) - \mathbf{V}$ ;

4   Form latent Jacobian  $\mathcal{J}_\alpha = \mathcal{J}_\sigma \mathcal{H}'(\mathbf{c}^k) \mathbf{B}$ ;

5   **repeat**

6     Solve LMF step:  $(\mathcal{J}_\alpha^\top \mathcal{J}_\alpha + \mu_k \mathbf{I}) \mathbf{d} = -\mathcal{J}_\alpha^\top \mathbf{r}^k$ ;

7      $\hat{\boldsymbol{\alpha}} = \boldsymbol{\alpha}^k + \mathbf{d}$ ;

8     Compute reduction ratio  $\rho_k$ ;

9     Update  $\mu_k$  according to (20);

10   **until**  $\rho_k > \rho_1$ ;

11   Accept the step;

12    $\boldsymbol{\alpha}^{k+1} = \hat{\boldsymbol{\alpha}}$ ;

13    $\mathbf{c}^{k+1} = \mathbf{B} \boldsymbol{\alpha}^{k+1}$ ;

14    $\boldsymbol{\sigma}^{k+1} = \mathcal{H}(\mathbf{c}^{k+1})$ ;

15    $k \leftarrow k + 1$ ;

16 **end**

17  $\hat{\boldsymbol{\sigma}} \leftarrow \boldsymbol{\sigma}^k$ ;

18 **return**  $\hat{\boldsymbol{\sigma}}$

---

### F. Computational Efficiency

BC-SR achieves computational efficiency through two design choices. First, the graph-Laplacian sparse representation reduces the optimization dimension from  $N$  to  $N_b$  ( $N_b \ll N$ ), thereby decreasing the cost of solving the normal equations. The basis  $\mathbf{B}$  is precomputed and fixed, and the bound mapping  $\mathcal{H}$  is applied componentwise. The latent Jacobian  $\mathcal{J}_\alpha = \mathcal{J}_\sigma \mathcal{H}'(\mathbf{c}) \mathbf{B}$  is assembled with minimal additional cost beyond  $\mathcal{J}_\sigma$ .

Second, BC-SR employs the LMF algorithm, requiring one solve of the damped normal equations per iteration (see (18)). In practice, convergence is achieved within approximately 10 iterations on the in-vivo data considered in this study.

The overall runtime can be approximated as

$$T \approx N_{\text{iter}}(T_{\text{fwd}} + T_J), \quad (21)$$

where  $T_{\text{fwd}}$  denotes forward/adjoint solves and  $T_J$  the Jacobian assembly cost.

## IV. EXPERIMENTAL SETUP

### A. Measurement Protocol and Evaluation Metrics

All experiments are conducted using a 16-electrode configuration. Adjacent current injection and adjacent voltage measurement patterns are adopted as the default protocol.

For numerical simulations (2D and 3D), all adjacent stimulation patterns are used together with adjacent voltage measurements. For the tank experiments, a subset of stimulation patterns is used by selecting electrodes  $\{1, 5, 9, 13\}$  as one terminal and enumerating all distinct pairings, resulting in 54

independent stimulation patterns. Adjacent voltage measurements are employed. For the in-vivo data, adjacent stimulation is applied, and voltage measurements involving current-driven electrodes are excluded. Reciprocal measurements are further removed, resulting in 104 independent measurements per frame.

Synthetic voltages  $\mathbf{V}$  are generated using the forward model in (2), with additive Gaussian noise corresponding to a signal-to-noise ratio (SNR) of 60 dB:

$$\text{SNR} = 10 \log_{10} \frac{\sum_i |\mathcal{U}(\boldsymbol{\sigma})_i|^2}{\sum_i |e_i|^2}. \quad (22)$$

To avoid inverse crimes, different FEM meshes are used for forward simulation and reconstruction. All conductivity values are reported in mS/cm. Reconstruction quality is evaluated using Structural Similarity Index (SSIM) [34], correlation coefficient (CC), and root mean square error (RMSE).

### B. Reconstruction Methods

We compare the proposed BC-SR method with conventional voxel-wise reconstruction approaches, including NOSER [7], iterative  $\ell_2$  [35], and TV [10], which are widely used and serve as standard baselines.

As a reference method for time-difference imaging, we adopt a linearized difference (LD) approach. The forward model is linearized around a baseline conductivity  $\boldsymbol{\sigma}_0$ :

$$\mathbf{V}_i \approx \mathbf{V}_0 + \mathbf{J}_0 \Delta \boldsymbol{\sigma}_i, \quad (23)$$

where  $\mathbf{J}_0$  denotes the Jacobian evaluated at  $\boldsymbol{\sigma}_0$ .

The reconstruction is obtained by solving the following regularized least-squares problem:

$$\widehat{\Delta \boldsymbol{\sigma}}_i = \arg \min_{\Delta \boldsymbol{\sigma}} \|\Delta \mathbf{V}_i - \mathbf{J}_0 \Delta \boldsymbol{\sigma}\|_2^2 + \alpha \Delta \boldsymbol{\sigma}^T \mathbf{R} \Delta \boldsymbol{\sigma}, \quad (24)$$

where  $\mathbf{R} = \text{diag}(\mathbf{J}_0^T \mathbf{J}_0)$  corresponds to a NOSER-type regularization. This formulation admits a closed-form solution of the form

$$\widehat{\Delta \boldsymbol{\sigma}}_i = (\mathbf{J}_0^T \mathbf{J}_0 + \alpha \mathbf{R})^{-1} \mathbf{J}_0^T \Delta \mathbf{V}_i = \mathbf{A} \Delta \mathbf{V}_i, \quad (25)$$

where  $\mathbf{A}$  is the corresponding linear reconstruction operator. In this work, this formulation is consistently referred to as the LD baseline in all numerical experiments.

In contrast, BC-SR performs nonlinear reconstruction in a low-dimensional latent space. For time-difference imaging, a warm-start strategy is adopted by initializing the target state with the baseline solution, which improves robustness to modeling mismatch and facilitates convergence.

### C. 2D Studies

**Ablation Study:** We conduct ablation experiments on a 2D phantom (Case 1; Fig. 3), consisting of three homogeneous regions with conductivities 0.25, 1.0, and 2.0 mS/cm.

Two aspects are evaluated: (i) constraint enforcement via nonlinear bound mapping (NLM) versus an active-set method (ASM), under fine bounds [0.2, 2.0] and coarse bounds [0.1, 4.0], and (ii) the effect of the graph-Laplacian sparse representation (SR) and basis truncation.

**2D Numerical Phantoms:** Four phantoms (Cases 2–5) are considered, covering smooth, sharp, high-contrast, and lung-like conductivity distributions. Two BC-SR variants are evaluated, which differ only in the conductivity bounds: BC-SR(F) uses accurate bounds consistent with the ground-truth range, while BC-SR(C) adopts relaxed bounds with a wider admissible interval.

**Noise Robustness Study:** To improve stability under noise, a lightweight TV term is incorporated, with its weight automatically scaled by the SNR:

$$\lambda(\text{SNR}) = \begin{cases} \lambda_0 (\sqrt{10})^{\frac{60-\text{SNR}}{10}}, & \text{SNR} < 60 \text{ dB}, \\ \lambda_0, & \text{SNR} \geq 60 \text{ dB}. \end{cases} \quad (26)$$

**Tank Experiments:** Experiments are conducted on a saline tank (28 cm diameter) with insulating inclusions. Five configurations (Tank 1–Tank 5) are evaluated, with conductivity bounds set to [0.001, 0.543] mS/cm. Data are acquired using the KIT4 system [36].

### D. 3D Studies

**3D Numerical Phantoms:** We evaluate BC-SR on two 3D phantoms (2.5D and full 3D), with conductivity settings summarized in Table I (see Fig. 2). Results are reported in a normalized coordinate system. Case 2.5D spans  $x \in [-0.945, 1.003]$ ,  $y \in [-0.651, 0.682]$ , and  $z \in [-0.5, 0.5]$ , while Case 3D uses  $x, y \in [-1, 1]$  and  $z \in [-0.8, 0.8]$ .

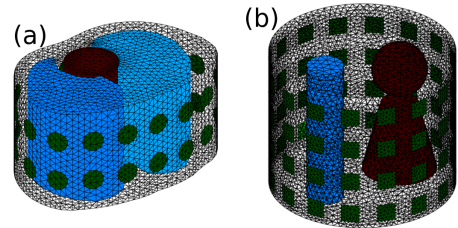


Fig. 2. 3D numerical phantoms and electrode configurations. Case 2.5D uses two electrode rings, and Case 3D uses four rings.

TABLE I  
CONDUCTIVITIES OF THE 3D NUMERICAL PHANTOMS (IN MS/CM).

Case	Background	Region A	Region B	Region C
2.5D	1.0	0.1 (left lung)	0.4 (right lung)	3.0 (heart)
3D	1.0	0.5 (cylinder)	5.0 (sphere)	5.0 (frustum)

**In-vivo Experiments:** The data was obtained from a previously reported in-vivo EIT–CT study, where ethical approval and informed consent were obtained [37]. The normalized domain spans  $x \in [-1, 1]$ ,  $y \in [-0.641, 0.641]$ , and  $z \in [-0.667, 0.667]$ . Conductivity bounds are set to [0.01, 8] mS/cm.

Time-difference imaging is performed over a respiratory cycle, with the end-expiration state ( $t_0 = 40.2$  s) as the baseline. For each frame  $t_i$ , the conductivity change is defined as

$$\Delta \boldsymbol{\sigma}_i = \boldsymbol{\sigma}_i - \boldsymbol{\sigma}_0. \quad (27)$$

## V. 2D RESULTS

### A. Ablation Study

1) *Impact of Representation Design*: Fig. 3 compares ASM and NLM, each with and without the sparse representation (SR). For SR variants, a fixed number of  $N_b = 200$  Laplacian eigenvectors is retained. With ASM, noticeable artifacts appear between adjacent regions, indicating cross-region leakage induced by the linearized parameterization. In contrast, NLM improves the separation between conductivity regions and yields clearer structural boundaries. When combined with SR, background fluctuations are further suppressed and the reconstructed shapes become more consistent with the ground truth. In particular, NLM+SR (BC-SR) achieves the most accurate geometry recovery, demonstrating improved structural fidelity under both fine and coarse conductivity bounds.

2) *Effect of Basis Truncation Level*: We further investigate the influence of the truncation level  $N_b$  in the graph-Laplacian basis. The full conductivity dimension is  $N = 2038$ , and  $N_b$  is selected as a fraction of  $N$ , corresponding to  $N_b \in \{50, 100, 200, 500, 1000\}$ . As shown in Fig. 4, the reconstruction quality is relatively insensitive to  $N_b$  over a wide range, especially when physically meaningful conductivity bounds are imposed. This indicates that the proposed representation is robust to moderate changes in model complexity. Based on this observation, we set  $N_b = 0.05N$  for the tank experiments and  $N_b = 0.1N$  for the 2D and 3D studies, providing a stable trade-off between accuracy and computational cost without case-specific tuning.

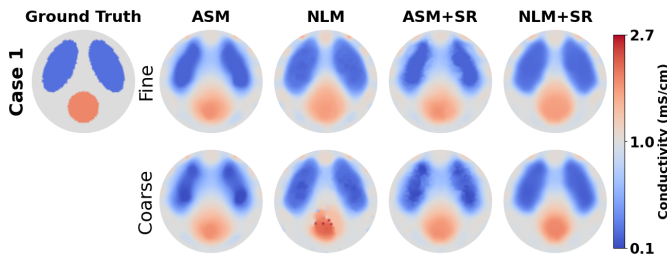


Fig. 3. Ablation study on ASM and NLM with SR. Rows correspond to fine and coarse bounds.

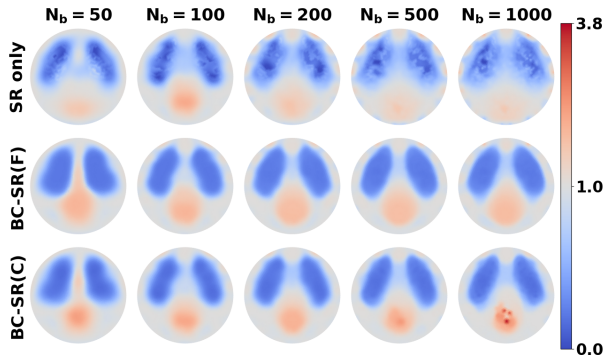


Fig. 4. Effect of Laplacian basis truncation level  $N_b$  on reconstruction performance.

### B. 2D Numerical Phantoms

Fig. 5 summarizes the reconstruction results for the 2D numerical phantoms. NOSER provides a coarse estimate of the conductivity distribution. L2 regularization produces smoother results but blurs sharp boundaries. TV improves edge preservation but may introduce staircase artifacts and fails in low-sensitivity regions, particularly in Case 4. In contrast, BC-SR achieves consistently better performance across all cases. It preserves sharp interfaces while maintaining smooth variations, successfully reconstructs the shielded structure in Case 4, and remains effective for smoothly varying distributions without relying on a piecewise-constant assumption. Table II reports SSIM, CC, and RMSE, providing quantitative support for the consistent performance of BC-SR.

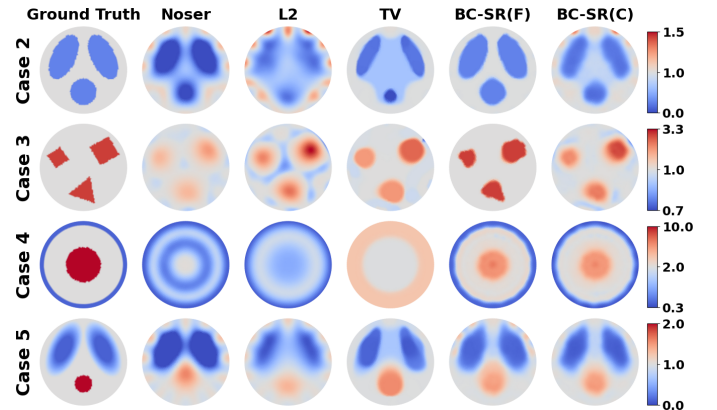


Fig. 5. Reconstruction results for the 2D numerical phantoms (Cases 2–5) at 60 dB noise. Each row corresponds to one phantom (Cases 2–5 from top to bottom). Columns show the ground truth (GT), Noser, L2, TV, BC-SR (F), and BC-SR (C).

TABLE II  
QUANTITATIVE METRICS OF RECONSTRUCTION RESULTS FOR CASES 2–5

Case	Metric	Noser	L2	TV	BC-SR(F)	BC-SR(C)
2	SSIM	0.470	0.513	0.656	<b>0.896</b>	0.666
	CC	0.891	0.902	0.897	<b>0.989</b>	0.954
	RMSE	0.111	0.072	0.074	<b>0.009</b>	0.035
3	SSIM	0.756	0.703	0.817	<b>0.879</b>	0.785
	CC	0.854	0.916	0.927	<b>0.950</b>	0.933
	RMSE	0.138	0.071	0.060	<b>0.039</b>	0.059
4	SSIM	0.655	0.708	0.460	0.724	<b>0.776</b>
	CC	0.627	0.379	0.055	0.911	<b>0.919</b>
	RMSE	0.633	0.661	0.737	<b>0.197</b>	0.202
5	SSIM	0.632	0.835	0.804	0.864	<b>0.881</b>
	CC	0.904	0.950	0.955	0.961	<b>0.970</b>
	RMSE	0.089	0.041	0.034	0.029	<b>0.023</b>

### C. Noise-Robustness Study

Fig. 6 reports Case 1 reconstructions at different noise levels using (26), and Table III summarizes SSIM, CC, and RMSE. As SNR decreases from 60 dB to 30 dB, image quality degrades smoothly and monotonically without abrupt failure, indicating robust behavior of BC-SR under measurement noise with the proposed SNR-driven TV weighting.

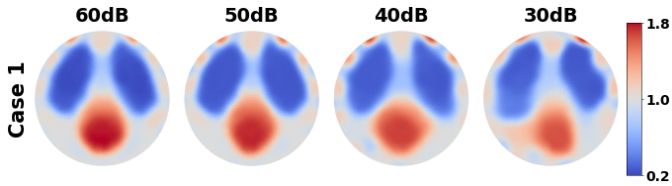


Fig. 6. Noise-robustness study on Case 1 using BC-SR with the SNR-adaptive TV weighting in (26). Columns correspond to different SNR levels (60, 50, 40, and 30 dB).

TABLE III

QUANTITATIVE METRICS FOR THE NOISE-ROBUSTNESS STUDY ON CASE 1 USING BC-SR WITH SNR-ADAPTIVE TV WEIGHTING.

SNR (dB)	SSIM	CC	RMSE
60	<b>0.737</b>	<b>0.961</b>	<b>0.031</b>
50	0.733	0.951	0.039
40	0.694	0.940	0.047
30	0.690	0.936	0.052

#### D. Tank Experiments

Fig. 7 compares reconstructions for five different tank experiments. NOSER is fast but produces blurred boundaries; L2 tends to oversmooth and merge nearby inclusions; TV preserves edges but may introduce staircase artifacts and shape distortions for irregular objects. BC-SR yields cleaner backgrounds and more accurate inclusion number and shape across all tank configurations.

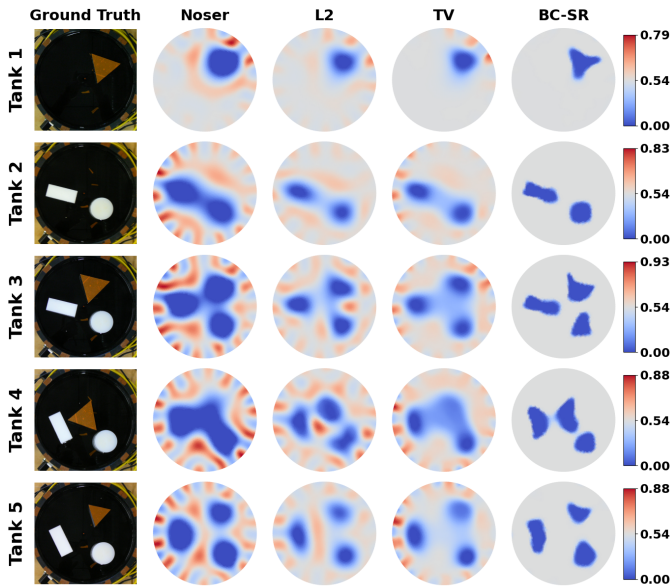


Fig. 7. Reconstruction results for five tank experiments with saline background and insulating agar inclusions. Each row corresponds to one tank configuration (Tank 1–Tank 5), and columns show reconstructions obtained by Noser, L2, TV, and BC-SR.

## VI. 3D RESULTS

### A. 3D Numerical Phantoms

1) *Case 2.5D*: We first consider the heart–lung phantom in Fig. 2(a), which is homogeneous along the  $z$ -direction. Each axial slice contains fixed left-lung, right-lung, and heart

regions with prescribed conductivities (Table I). Representative axial slices are shown in Fig. 8.

NOSER captures the overall organ structure but exhibits limited spatial resolution and amplitude bias. TV improves structural delineation but tends to shrink lung regions and underestimate the heart conductivity. In comparison, BC-SR achieves more accurate shape and intensity reconstruction, with only minor residual non-uniformity in the right lung.

2) *Case 3D*: We next evaluate a fully 3D phantom with strong  $z$ -variation (Fig. 2(b)), consisting of a low-conductivity cylinder and two high-conductivity inclusions (a sphere and a frustum) embedded in a homogeneous background. Representative axial, coronal, and sagittal slices are shown in Fig. 9.

NOSER fails to recover the full 3D structure, particularly underestimating high-conductivity regions. TV partially restores the lower inclusion but struggles with the upper sphere. BC-SR consistently reconstructs both inclusions with more accurate geometry and conductivity levels, achieving the best overall balance between structural fidelity and quantitative accuracy.

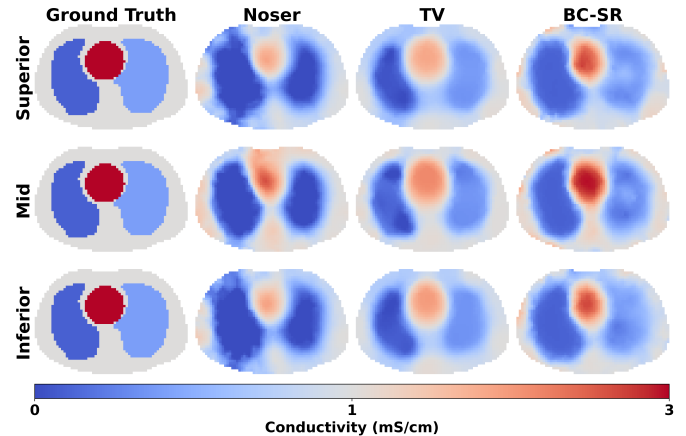


Fig. 8. 3D simulation results for Case 2.5D. From top to bottom, three axial slices at normalized positions  $z = 0.4$ ,  $z = 0.0$ , and  $z = -0.4$  are shown for the ground truth and the reconstructions obtained by Noser, TV, and BC-SR.

### B. In-vivo Experiments

Fig. 10 summarizes the results from three complementary perspectives: (a) spatial reconstruction, (b) anatomical reference, and (c) temporal ventilation analysis. Fig. 10(a) compares the reconstructed 3D conductivity distributions obtained by LD and BC-SR. LD provides a qualitatively interpretable reconstruction but exhibits strong smoothing effects and limited spatial consistency across slices. In contrast, BC-SR yields more coherent and spatially consistent 3D structures across axial ( $z = 0$ ), coronal ( $y = 0$ ), and sagittal ( $x = -0.3$ ) views, enabled by its global 3D basis representation with bound-constrained parameterization, which inherently promotes structured and spatially coherent volumetric distributions beyond slice-wise or plane-dominated reconstructions. Due to the ill-posed nature of EIT, regions away from the electrode plane are inherently weakly constrained by measurements. In this context, the reconstruction is governed by

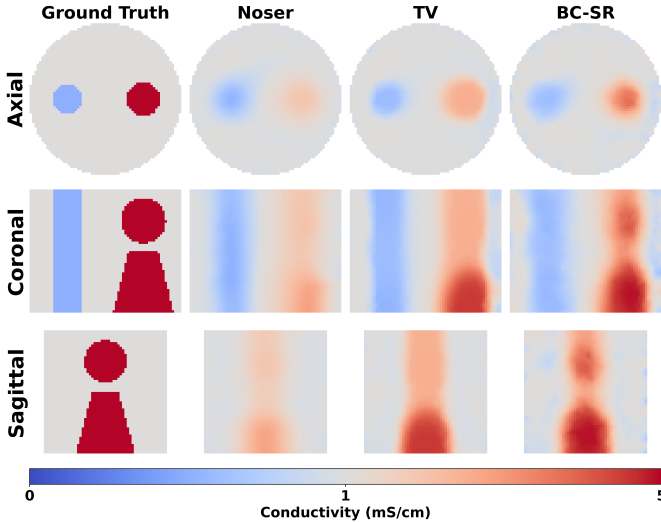


Fig. 9. 3D simulation results for Case 3D. An axial slice at  $z = 0.2$ , a coronal slice at  $y = 0$ , and a sagittal slice at  $x = 0.6$  are shown for the ground truth and the reconstructions obtained by Noser, TV, and BC-SR.

the global low-frequency 3D representation, and the resulting off-plane structures should be interpreted as physics-consistent volumetric inferences induced by the model, rather than direct observations or reconstruction artifacts. Fig. 10(b) presents CT slices ((i)–(iii)) as anatomical references for qualitative assessment of lung morphology, since no ground-truth conductivity is available in in-vivo measurements. The FEM mesh used for EIT modeling is also shown in (iv). BC-SR demonstrates better agreement with the expected lung anatomy at end-inspiration (41.1 s), while LD exhibits noticeable geometric distortions, including overextension of high-conductivity regions toward the boundary. To further analyze functional ventilation dynamics, we define a lung ventilation index  $F_\Omega$  over a region  $\Omega$  by integrating conductivity decreases during the respiratory cycle:

$$F_\Omega = \sum_{\Gamma \in \Omega} [-\overline{\Delta\sigma_\Gamma}]_+ \nu_\Gamma, \quad (28)$$

Let  $\mathcal{N}_\Gamma$  denote the set of nodes associated with element  $\Gamma$ , and define  $N_\Gamma = |\mathcal{N}_\Gamma|$  as the number of nodes. The element-wise mean conductivity change is then given by

$$\overline{\Delta\sigma_\Gamma} = \frac{1}{N_\Gamma} \sum_{j \in \mathcal{N}_\Gamma} \Delta\sigma_j. \quad (29)$$

Fig. 10(c) shows the temporal evolution of the ventilation index  $F_\Omega$  over a full breathing cycle. Ventilation increases in both lungs during inspiration, with a faster rise in the right lung. The peak occurs at 41.1 s, with left and right contributions of 41.1% and 58.9%, respectively. The inspiration-to-expiration duration ratio is approximately 1 : 1.7.

This left–right distribution is physiologically consistent with lung anatomy: the right lung (three lobes) generally has greater volume and ventilation capacity than the left (two lobes) [38], with typical volume ratios of 40%–45% (left) and 55%–60% (right) [39]. The BC-SR results fall within this range, supporting their quantitative validity. In contrast, LD relies on local linearization and shows reduced temporal stability,

limiting its suitability for volumetric analysis. Consequently, the proposed 3D ventilation index is not evaluated for LD.

## VII. DISCUSSION

The proposed BC-SR framework integrates structural priors and physical constraints through a nonlinear parameterization, enabling improved stability and reconstruction quality across a range of EIT scenarios. The in-vivo results further demonstrate its potential for quantitative 3D difference imaging under realistic measurement conditions. A key advantage of the proposed formulation lies in its representation-driven design. By restricting the solution space through a low-dimensional basis and enforcing admissible conductivity ranges via a nonlinear mapping, BC-SR improves conditioning and reduces the sensitivity to noise and modeling errors. In particular, the warm-start strategy aligns the reconstruction with the baseline state, thereby reducing shared modeling errors and improving robustness in time-difference imaging.

Despite these advantages, several aspects merit further consideration. First, the reconstruction performance depends on the choice of conductivity bounds, which are assumed to be known or estimated as a prior. While the method is relatively robust to moderate bound variations, overly restrictive or excessively loose bounds may affect reconstruction accuracy. Another aspect is that the expressiveness of the representation is controlled by the number of retained basis functions  $N_b$ , which governs the trade-off among reconstruction fidelity, computational efficiency, and robustness. Although the proposed method is stable across a wide range of  $N_b$ , larger values increase representation capacity but may lead to overfitting, particularly in noisy settings. The current framework also relies on a fixed graph-based basis derived from mesh connectivity. While this provides a generic and geometry-consistent prior, it does not explicitly adapt to problem-specific features or anatomical structures. Incorporating adaptive or data-driven basis constructions could further enhance representation capability. Lastly, the computational cost of the nonlinear optimization is higher than that of linearized methods such as the LD baseline, which may limit real-time applications. However, the improved reconstruction accuracy and robustness may justify this trade-off in applications requiring quantitative analysis. Future work will focus on adaptive basis design, improved initialization strategies, and efficient implementations for real-time clinical deployment.

## VIII. CONCLUSION

We proposed BC-SR, a novel EIT reconstruction framework based on Bound-Constrained Sparse Representation. By integrating structural priors and physical constraints through a bound-preserving mapping and a truncated graph-Laplacian basis, BC-SR eliminates the need for explicit regularization. This formulation ensures stable and robust reconstructions even in the presence of noise and modeling mismatches, and supports both absolute and time-difference imaging in a unified framework. Extensive validation through 2D/3D simulations, tank experiments, and in-vivo data demonstrates that BC-SR significantly improves structural fidelity and

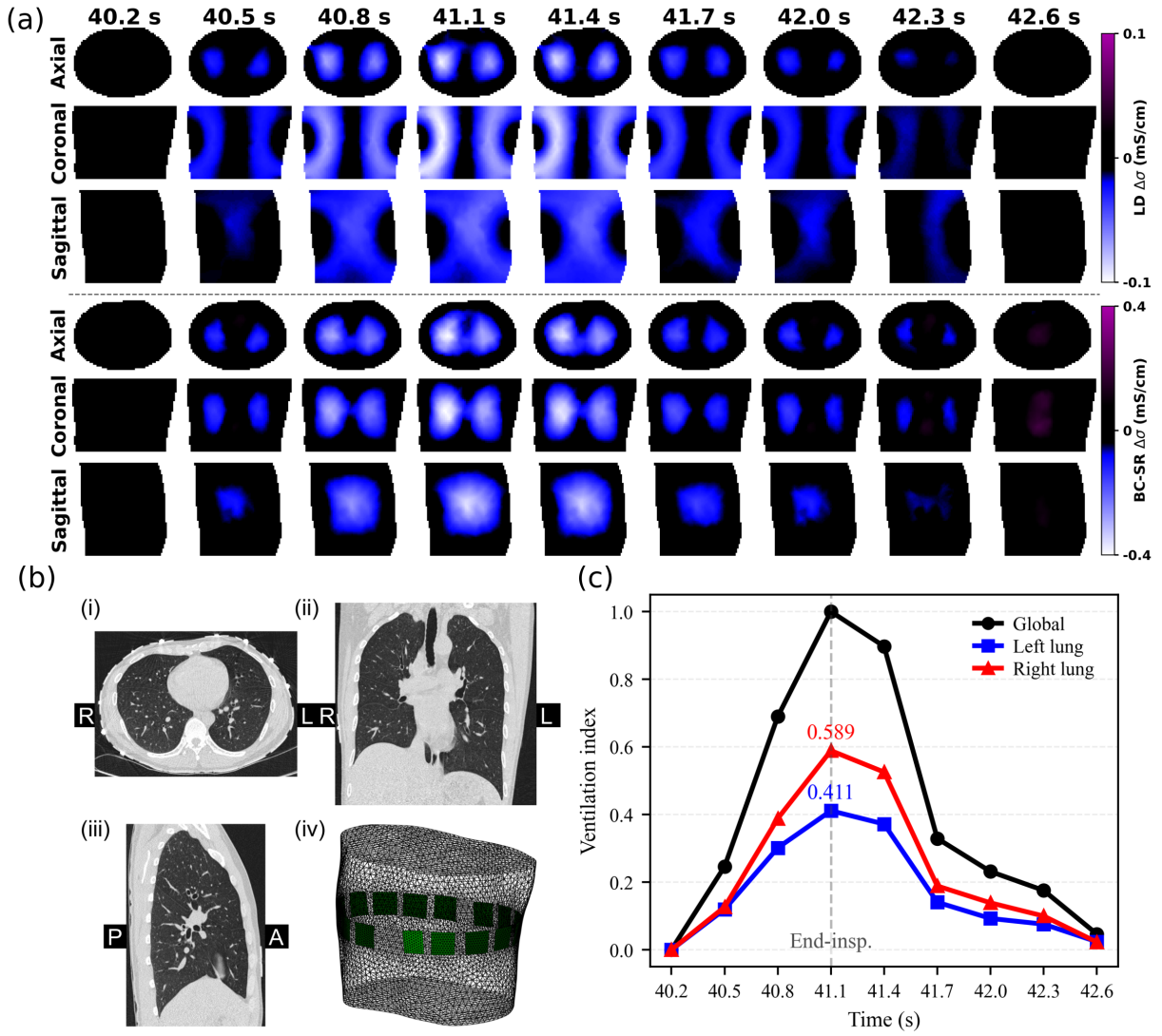


Fig. 10. In-vivo time-difference imaging results over a full breathing cycle. (a) Comparison between linear difference (LD) with NOSER-type regularization and the proposed BC-SR method. BC-SR provides a 3D conductivity reconstruction, visualized by axial ( $z = 0$ ), coronal ( $y = 0$ ), and sagittal ( $x = -0.3$ ) slices. (b) Corresponding CT slices ((i)–(iii)) for anatomical reference, along with the FEM mesh (iv). (c) Temporal evolution of the lung ventilation index  $F_{\Omega}$  over the respiratory cycle.

quantitative consistency compared to conventional methods. These results highlight BC-SR’s potential for reliable, robust ventilation-related analysis, particularly in clinical applications. The flexibility of the BC-SR framework, combined with its physics-consistent approach, makes it a promising tool for addressing other nonlinear inverse problems with boundary measurements.

#### ACKNOWLEDGMENT

The authors would like to sincerely thank Professor Maokun Li from the Department of Electronic Engineering, Tsinghua University, for providing the in-vivo data used in this study. The authors also thank Junwu Wang for providing the 3D forward-solver code and for helpful discussions, and Bowen Tong for valuable comments and suggestions.

#### REFERENCES

- [1] S. Qu, E. Feng, D. Dong, L. Yang, M. Dai, I. Frerichs, S. Liu, Y. Gao, J. Zheng, L. Song *et al.*, “Early screening of lung function by electrical impedance tomography in people with normal spirometry reveals unrecognized pathological features,” *Nature Communications*, vol. 16, no. 1, p. 622, 2025.
- [2] O. Brabant, B. Crivellari, G. Hosgood, A. Raisis, A. Waldmann, U. Auer, A. Adler, L. Smart, M. Laurence, and M. Mosing, “Effects of peep on the relationship between tidal volume and total impedance change measured via electrical impedance tomography (eit),” *Journal of Clinical Monitoring and Computing*, vol. 36, no. 2, pp. 325–334, 2022.
- [3] M. C. Bachmann, C. Morais, G. Bugeo, A. Bruhn, A. Morales, J. B. Borges, E. Costa, and J. Retamal, “Electrical impedance tomography in acute respiratory distress syndrome,” *Critical Care*, vol. 22, no. 1, p. 263, 2018.
- [4] L. Cao, H. Li, D. Fu, X. Liu, H. Ma, C. Xu, X. Dong, B. Yang, and F. Fu, “Real-time imaging of infarction deterioration after ischemic stroke in rats using electrical impedance tomography,” *Physiological Measurement*, vol. 41, no. 1, p. 015004, 2020.
- [5] A. Hauptmann, M. Santacesaria, and S. Siltanen, “Direct inversion from partial-boundary data in electrical impedance tomography,” *Inverse Problems*, vol. 33, no. 2, p. 025009, 2017.

- [6] B. Brazey, Y. Haddab, and N. Zemiti, "Robust imaging using electrical impedance tomography: review of current tools," *Proceedings of the Royal Society A*, vol. 478, no. 2258, p. 20210713, 2022.
- [7] M. Cheney, D. Isaacson, J. C. Newell, S. Simske, and J. Goble, "Noser: An algorithm for solving the inverse conductivity problem," *International Journal of Imaging systems and technology*, vol. 2, no. 2, pp. 66–75, 1990.
- [8] A. Adler, J. H. Arnold, R. Bayford, A. Borsic, B. Brown, P. Dixon, T. J. Faes, I. Frerichs, H. Gagnon, Y. Gärber *et al.*, "Greit: a unified approach to 2d linear eit reconstruction of lung images," *Physiological measurement*, vol. 30, no. 6, p. S35, 2009.
- [9] B. Grychtol, B. Müller, and A. Adler, "3d eit image reconstruction with greit," *Physiological measurement*, vol. 37, no. 6, p. 785, 2016.
- [10] A. Borsic, B. M. Graham, A. Adler, and W. R. Lionheart, "In vivo impedance imaging with total variation regularization," *IEEE transactions on medical imaging*, vol. 29, no. 1, pp. 44–54, 2009.
- [11] G. González, V. Kolehmainen, and A. Seppänen, "Isotropic and anisotropic total variation regularization in electrical impedance tomography," *Computers & Mathematics with Applications*, vol. 74, no. 3, pp. 564–576, 2017.
- [12] Y. Wu, B. Chen, K. Liu, S. Huang, Y. Li, J. Jia, and J. Yao, "Bayesian image reconstruction using weighted laplace prior for lung respiratory monitoring with electrical impedance tomography," *IEEE Transactions on Instrumentation and Measurement*, vol. 72, pp. 1–11, 2022.
- [13] B. Gong, B. Schullcke, S. Krueger-Ziolek, M. Vauhkonen, G. Wolf, U. Mueller-Lisse, and K. Moeller, "Eit imaging regularization based on spectral graph wavelets," *IEEE transactions on medical imaging*, vol. 36, no. 9, pp. 1832–1844, 2017.
- [14] S. Liu, J. Jia, Y. D. Zhang, and Y. Yang, "Image reconstruction in electrical impedance tomography based on structure-aware sparse bayesian learning," *IEEE transactions on medical imaging*, vol. 37, no. 9, pp. 2090–2102, 2018.
- [15] B. Schullcke, B. Gong, S. Krueger-Ziolek, M. Soleimani, U. Mueller-Lisse, and K. Moeller, "Structural-functional lung imaging using a combined ct-eit and a discrete cosine transformation reconstruction method," *Scientific reports*, vol. 6, no. 1, p. 25951, 2016.
- [16] K. W. See, K.-S. Loke, P. A. Lee, and K.-F. Loe, "Image reconstruction using various discrete orthogonal polynomials in comparison with dct," *Applied Mathematics and Computation*, vol. 193, no. 2, pp. 346–359, 2007.
- [17] W. Zhang, J. Gao, Y. Yang, D. Liang, X. Liu, H. Zheng, and Z. Hu, "Image reconstruction for positron emission tomography based on patch-based regularization and dictionary learning," *Medical physics*, vol. 46, no. 11, pp. 5014–5026, 2019.
- [18] Q. Wang, X. Ding, M. Ma, X. Li, X. Duan, and J. Wang, "Research on sparse imaging method of electrical impedance tomography based on dk-svd," *Progress in Electromagnetics Research M*, vol. 114, 2022.
- [19] D. Liu, D. Gu, D. Smyl, A. K. Khambampati, J. Deng, and J. Du, "Shape-driven eit reconstruction using fourier representations," *IEEE Transactions on Medical Imaging*, vol. 40, no. 2, pp. 481–490, 2020.
- [20] S. Ren, K. Sun, D. Liu, and F. Dong, "A statistical shape-constrained reconstruction framework for electrical impedance tomography," *IEEE Transactions on Medical Imaging*, vol. 38, no. 10, pp. 2400–2410, 2019.
- [21] D. Liu, D. Smyl, and J. Du, "A parametric level set-based approach to difference imaging in electrical impedance tomography," *IEEE transactions on medical imaging*, vol. 38, no. 1, pp. 145–155, 2018.
- [22] D. Liu, H. Xia, C. Wang, H. Xiang, Y. Huang, and S. K. Zhou, "Gsr: A gaussian splatting-based reconstruction framework for eit," *IEEE Transactions on Medical Imaging*, 2025.
- [23] J. K. Seo, K. C. Kim, A. Jargal, K. Lee, and B. Harrach, "A learning-based method for solving ill-posed nonlinear inverse problems: A simulation study of lung eit," *SIAM journal on Imaging Sciences*, vol. 12, no. 3, pp. 1275–1295, 2019.
- [24] Z. Lin, R. Guo, K. Zhang, M. Li, F. Yang, S. Xu, D. Liu, and A. Abubakar, "Feature-based inversion using variational autoencoder for electrical impedance tomography," *IEEE Transactions on Instrumentation and Measurement*, vol. 71, pp. 1–12, 2022.
- [25] D. Liu, J. Wang, Q. Shan, D. Smyl, J. Deng, and J. Du, "Deepeit: Deep image prior enabled electrical impedance tomography," *IEEE Transactions on Pattern Analysis and Machine Intelligence*, vol. 45, no. 8, pp. 9627–9638, 2023.
- [26] J. Wang, Y. Wang, J. Deng, and D. Liu, "Unsupervised coordinate-based neural network for electrical impedance tomography," *IEEE Transactions on Computational Imaging*, vol. 9, pp. 1213–1225, 2023.
- [27] C. Wang, H. Deng, and D. Liu, "Physics-driven neural compensation for electrical impedance tomography," *IEEE Transactions on Pattern Analysis and Machine Intelligence*, pp. 1–18, 2025.
- [28] A. Pokkunuru, P. Rooshenas, T. Strauss, A. Abhishek, and T. Khan, "Improved training of physics-informed neural networks using energy-based priors: a study on electrical impedance tomography," in *The Eleventh International Conference on Learning Representations*, 2023. [Online]. Available: <https://openreview.net/forum?id=zqkfJA6R1-r>
- [29] Z. Zhu, Z. Zhang, Z. Wang, Z. Yuan, X. Zhao, A. Ma, J. Sun, L. Xu, and L. Mo, "Pgct-pinn: A physics-guided cooperative training framework for enhanced resolution and consistency in lung eit imaging," *IEEE Internet of Things Journal*, vol. 13, no. 8, pp. 17631–17642, 2026.
- [30] D. Smyl, T. N. Tallman, L. Homa, C. Flournoy, S. J. Hamilton, and J. Wertz, "Physics informed neural networks for electrical impedance tomography," *Neural Networks*, vol. 188, p. 107410, 2025.
- [31] K.-S. Cheng, D. Isaacson, J. Newell, and D. G. Gisser, "Electrode models for electric current computed tomography," *IEEE transactions on biomedical engineering*, vol. 36, no. 9, pp. 918–924, 1989.
- [32] P. J. Vauhkonen, M. Vauhkonen, T. Savolainen, and J. P. Kaipio, "Three-dimensional electrical impedance tomography based on the complete electrode model," *IEEE Transactions on Biomedical Engineering*, vol. 46, no. 9, pp. 1150–1160, 2002.
- [33] R. Fletcher, *Practical Methods of Optimization*. John Wiley & Sons, 2013.
- [34] Z. Wang, A. C. Bovik, H. R. Sheikh, and E. P. Simoncelli, "Image quality assessment: From error visibility to structural similarity," *IEEE Transactions on Image Processing*, vol. 13, no. 4, pp. 600–612, 2004.
- [35] P. Hua, E. J. Woo, J. G. Webster, and W. J. Tompkins, "Iterative reconstruction methods using regularization and optimal current patterns in electrical impedance tomography," *IEEE Transactions on Medical Imaging*, vol. 10, no. 4, pp. 621–628, 1991.
- [36] J. Kourunen, T. Savolainen, A. Lehtikainen, M. Vauhkonen, and L. Heikkinen, "Suitability of a pxi platform for an electrical impedance tomography system," *Measurement Science and Technology*, vol. 20, no. 1, p. 015503, 2008.
- [37] K. Zhang, R. Guo, M. Li, F. Yang, S. Xu, and A. Abubakar, "Supervised descent learning for thoracic electrical impedance tomography," *IEEE Transactions on Biomedical Engineering*, vol. 68, no. 4, pp. 1360–1369, 2020.
- [38] J. B. West and A. M. Luks, *West's respiratory physiology*. Lippincott Williams & Wilkins, 2020.
- [39] J. F. Nunn, *Applied respiratory physiology*. Butterworth-Heinemann, 2013.